ChemComm

COMMUNICATION

View Article Online
View Journal | View Issue

Cite this: *Chem. Commun.*, 2016, 52, 7998

Received 5th May 2016,
Accepted 23rd May 2016

DOI: 10.1039/c6cc03768b

www.rsc.org/chemcomm

3D hierarchical MnO_2 nanorod/welded Ag-nanowire-network composites for high-performance supercapacitor electrodes†

Zhensong Qiao,[a] Xiaopeng Yang,*[a] Shuhua Yang,[a] Liqiang Zhang[b] and Bingqiang Cao*[a]

3D MnO_2 nanorod/welded Ag-nanowire-network supercapacitor electrodes were prepared. Welding treatment of the Ag nanowire-network leads to low resistance and long lifetime. Galvanostatic charge/discharge (GCD) induces an ever-lasting morphology changing from flower-like to honeycomb-like for MnO_2, which manifests as increasing specific capacitance to 663.4 F g^{-1} after 7000 GCD cycles.

Development of alternative energy sources and energy storage devices is of great importance globally, because of the urgent need to replace rapidly consumed fossil fuels and to alleviate climate change. Supercapacitors (SCs) are promising energy storage devices, which have drawn increasing attention because of their unique features of high power density, fast charge/discharge rate, and long-term stability.[1,2] To further improve the electrochemical performance of SCs, development of high-performance electrode materials is vitally important. In general, the most widely used electrodes for SCs are carbon material, transition-metal oxides, and conducting polymers. The transition-metal oxides such as RuO_2, NiO, MnO_2, Co_3O_4 and Fe_3O_4 are promising electrode materials because of their high specific capacitances from the fast and reversible redox reactions on the material surface.[3]

Among the various transition-metal oxide electrode materials, MnO_2 is an attractive pseudocapacitive material with high theoretical specific capacitance (up to 1370 F g^{-1}), and it is low cost, naturally abundant, and environmentally friendly.[4,5] However, the poor conductivity (10^{-5}–10^{-6} S cm^{-1}) of MnO_2 has limited development of MnO_2-based SCs with high capacity performance.[6] In recent years, two strategies have been developed to improve the conductivity of MnO_2. The first is doping various elements to form a mixed oxides matrix.[7] The second is to combine MnO_2 with a material with excellent conductivity, such as a carbon material, metal, or oxides.[4,8,9] Among conductive materials studied, Ag shows promise as a collector material for an MnO_2-based electrode.[10,11] Recent investigations have shown that nanostructure Ag, in particular Ag nanowires (AgNW), can improve the electrochemical performance of MnO_2-based SCs. Xia *et al.* reported an electrode with hierarchical heterostructure of Ag/MnO_2 nanowires, which exhibited much larger specific capacitances compared with bare MnO_2.[3] Thomas *et al.* prepared sandwich-like AgNW/PEDOT:PSS nanopillar/MnO_2 for SC electrodes, exhibiting enhanced capacitive performance.[12] Tay *et al.* reported a ternary hybrid electrode fabricated with 2-D graphene, MnO_2 and AgNW, which also showed superior capacity performance.[13] Hence, the AgNW can significantly boost the surface and the conductivity of MnO_2. However, poor adhesion of the AgNWs means that they can be lost easily by peeling off in the electrolyte. This severely impacts the deposition quality of MnO_2 on AgNWs and reduces the lifetime of AgNW/MnO_2-based SC electrodes.

Herein, as a possible SC electrode material with high capacitive performance, we first report the three-dimensional (3D) flower-like MnO_2 nanostructure grown directly on a welded AgNW network by an electrochemical deposition method. The welded AgNW network can form junctions at AgNW crossing points to prevent peeling off of the AgNWs, resulting in long-term stability of the 3D hierarchical MnO_2 nanorod/welded Ag-nanowire-network (MN/w-ANN) electrode with more than 7000 GCD cycles. The 3D MN/w-ANN electrode shows ever-increasing specific capacitance (from 423.5 F g^{-1} up to 663.4 F g^{-1}) because of the gradual morphology changing from flower-like to honeycomb-like MnO_2 with increasing galvanostatic charge/discharge (GCD) number.

The steps involved in fabrication of the SC electrodes (Fig. 1) are presented. The ultralong AgNWs were synthesized by reducing $AgNO_3$ with ethylene glycol (EG) in the presence of polyvinylpyrrolidone (PVP) and $FeCl_3$, as described previously.[14] Then, AgNW ink was spun on the surface of FTO substrates at 3000 rpm several times to ensure the AgNW network layer was dense enough. Next, the AgNW network was welded at different annealing temperature for 30 min under an Ar atmosphere to

[a] *Laboratory of Inorganic Energy and Environment Materials, School of Material Science and Engineering, University of Jinan, Jinan 250022, Shandong, China. E-mail: mse_yangxp@ujn.edu.cn, mse_caobq@ujn.edu.cn; Fax: +86-0531-89736292; Tel: +86-0531-89736292*

[b] *State Key Laboratory of Heavy Oil Processing and Department of Materials Science and Engineering, China University of Petroleum, Beijing 102249, China*

† Electronic supplementary information (ESI) available: XRD, SEM and CV dates. See DOI: 10.1039/c6cc03768b

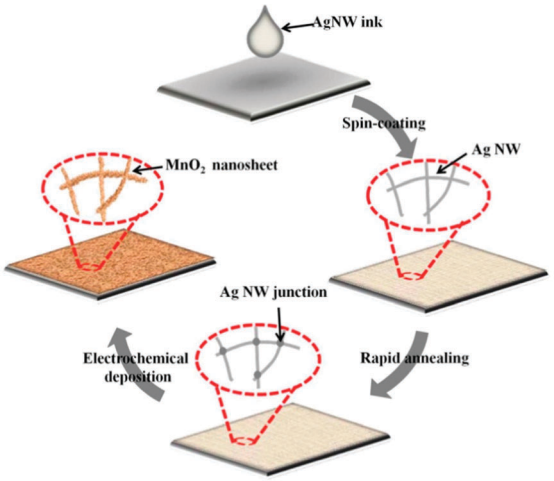

Fig. 1 Fabrication procedures for 3D MN/w-ANN composite electrodes on FTO substrate.

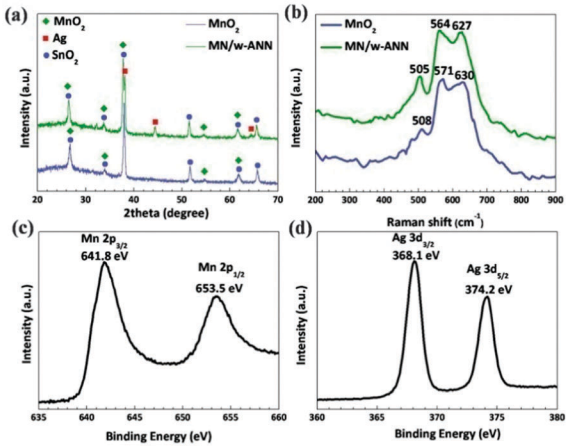

Fig. 2 (a) XRD patterns of bare MnO_2 and 3D MN/w-ANN composites. (b) Raman spectra of bare MnO_2 and 3D MN/w-ANN composites. (c) and (d) XPS core-level spectra of Mn 2p, and Ag 3d of the3D MN/w-ANN composite, respectively.

form junctions between AgNWs. Electrodeposition of MnO_2 was carried out in 0.25 M $Mn(CH_3COO)_2{\cdot}4H_2O$ solution by a potentiostatic electrochemical deposition technique with three electrode configuration. Carbon, saturated calomel, and AgNW/FTO substrates were used as the counter electrode, reference electrode, and working electrode, respectively. The portion of the working electrodes at which the MnO_2 was to be deposited was dipped into the solution, with the remainder of the AgNW/FTO kept in air. A 0.45 V potential was applied to the electrode for 400 seconds. The final 3D MN/w-ANN composites were washed in distilled water three times. The loading mass of the plated MnO_2 was calculated by integrating the total coulombic charges used for plating over electrolysis durations, and was confirmed by direct weight measurements of the electrodes (see the ESI†).[7]

Morphology and crystal structure studies were performed on the samples using field emission scanning electron microscopy (SEM, Quanta 250, FEI), transmission electron microscopy (TEM, Tecnai G2 F20, FEI), X-ray photoelectron spectroscopy (XPS, Thermo Fisher K-Alpha American with an Al Kα X-ray source), high resolution Raman spectrometry (LabRAM HR Evolution, HORIBA JOBIN YVON S. A. S), and X-ray diffraction (XRD, D8-Advance, Bruker). Cyclic voltammetry (CV), GCD, and electrochemical impedance spectroscopy (EIS) were carried out in a three-electrode system using an electrochemical workstation (Zahner/Zennium E 6.0). The electrolyte was a 0.5 M Na_2SO_4 aqueous solution.

The XRD pattern of AgNW/FTO substrate (Fig. S1a, ESI†) shows the presence of metallic Ag (JCPDFS 87-0597) and cassiterite SnO_2 (JCPDFS 77-0452) from the FTO substrate. In the two patterns shown in Fig. 2a, the diffraction peaks at 26.6°, 34°, 37.9°, 54.8°, and 61.6° indicate the ramsdellite MnO_2 (JCPDFS 42-1316), and the peaks at 26.5°, 33.7°, 37.8°, 51.6°, 61.6°, and 65.7° are the characteristic peaks of cassiterite SnO_2. In the green curve, three new diffraction peaks are observed at about 38.1°, 44.3°, and 64.4°, which index the (111), (200), and (220) peaks of metallic Ag. The structural assignment is further corroborated by Raman spectroscopic analysis (Fig. 2b). The peaks at 508, 570, 630 cm^{-1} of bare MnO_2 and the peaks at 505, 564, 627 cm^{-1} of the MN/w-ANN electrode demonstrate that the deposited MnO_2 is ramsdellite MnO_2.[15]

The chemical compositions and surface chemical states of the 3D MN/w-ANN composites were examined by XPS. Four elements (C, Ag, Mn, and O) were identified from the full-survey-scan spectrum of the 3D MN/w-ANN composite (Fig. S1b, ESI†). The Mn 3s spectrum (Fig. S1c, ESI†) shows a peak separation value of 4.83 eV, suggesting that Mn^{4+} is the dominant Mn species.[16] In Fig. 2c, two distinct peaks with binding energies of 641.8 and 653.5 eV can be assigned to Mn $2p_{1/2}$ and Mn $2p_{3/2}$, respectively, indicating that Mn mainly exists in the form of Mn^{4+} in the 3D MN/w-ANN composites.[3] The Ag 3d spectrum (Fig. 2d) shows two obvious peaks located at 368.1 eV for Ag $2d_{3/2}$ and 374.2 eV for Ag $2d_{5/2}$, with a spin energy separation of 6.1 eV, which indicates that Ag is present in the metallic state.[10]

Fig. 3a–d and Fig. S2 (ESI†) show SEM images of the AgNW network, the bare MnO_2, and the 3D MN/w-ANN samples. According to Fig. 3a and Fig. S2a and b, (ESI†), the interconnected ultralong AgNWs form a good 3D network. The diameters range from 40 nm to 200 nm. Based on the morphologic features, the AgNW network not only facilitates electron transfer but also provides a large surface

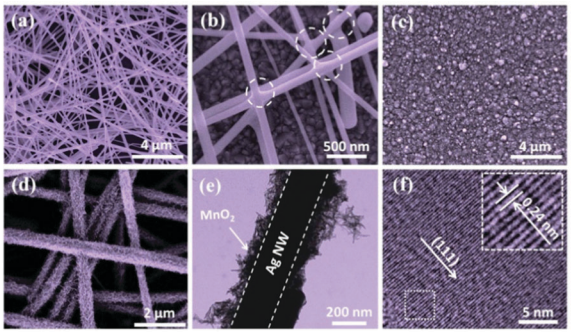

Fig. 3 SEM images of (a) AgNW network, (b) annealing AgNW network, (c) bare MnO_2 film on FTO, (d) 3D MN/w-ANN composites. (e) and (f) TEM images of the 3D MN/w-ANN composites.

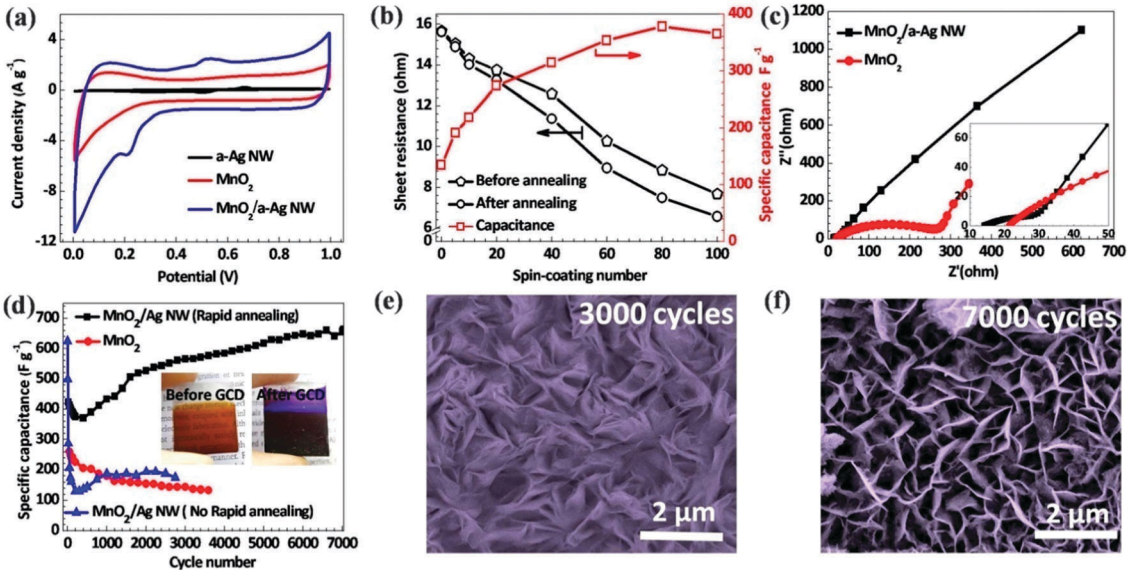

Fig. 4 (a) CV curves of the a-AgNW electrode, the bare MnO_2, and the 3D MN/w-ANN electrodes at a scan rate of 5 mV s^{-1}. (b) Specific capacitances of 3D MN/w-ANN electrodes and the sheet resistances of AgNW/FTO substrates at different spin-coating number before and after annealing treatment. (c) EIS of 3D MnO_2/a-AgNW and the bare MnO_2 electrodes, the inset shows the enlarged EIS at the high-frequency region. (d) Cycling performance at a current of 0.5 mA (red curve: the bare MnO_2; black and blue curves: the MN/ANN and MN/w-ANN electrodes, respectively). The insets are optical images of the 3D MN/w-ANN electrodes before and after GCD. (e) SEM image of the 3D MN/w-ANN electrode after 3000-cycle GCD measurement. (f) SEM image of the 3D MN/w-ANN electrode after 7000-cycle GCD measurement.

area. For the initial AgNW network, the connections at the crossed section are established by physical contacts, such as van der Waals forces and capillary force from solvent evaporation.[17,18] Thus, the AgNW network can be lost easily by peeling off in the electrolyte. To solve this problem, AgNW networks were welded at 200, 250, 300 and 350 °C for 30 minutes under an Ar atmosphere to form junctions at the crossing points of AgNWs. At 200 °C, the AgNWs could not be welded together (Fig. S2c, ESI†). Up to 250 °C, only slim AgNWs welded together (Fig. S2d, ESI†), probably because the annealing temperature was not high enough. Junctions were formed with various diameters at 300 °C (marked by the dashed circles in Fig. 3b and Fig. S2e, ESI†). However, at 350 °C the AgNWs suffered serious distortion and fused together, which caused destruction of the AgNW network (Fig. S2f, ESI†). Thus, the optimal annealing temperature at which to form AgNW junctions is 300 °C.

Based on Fig. 3c, MnO_2 particle islands are deposited on the surface of FTO to form a compact MnO_2 film, with small surface area. By contrast, Fig. 3d shows a dramatically different MnO_2 product with a flower-like morphology coated on the AgNWs to form 3D hierarchical MN/w-ANN composites. The detailed microstructure of the MN/w-ANN composite is shown in the TEM images. Fig. 3e shows a magnified image of MnO_2 deposited on the surface of AgNWs, and the flower-like MnO_2 coating is composed of nanorods. Therefore, the 3D hierarchical MN/w-ANN composite has large surface area; however, because of the low mass loading of the study material, reliable BET measurements were not possible.[19] A representative high-resolution TEM image (Fig. 3f) displays the distinct lattice fringes with an interlayer spacing of 0.24 nm, which are indexed to (111) planes of ramsdellite MnO_2. The energy dispersive X-ray spectrometry (EDS) spectrum (Fig. S3, ESI†) exhibits peaks of C, O, Mn, Ag, and Sn, supporting the incorporation of MnO_2, AgNWs, and SnO_2. The insets of Fig. S3 (ESI†) are the element mapping of Mn, Sn, and Ag, indicating that AgNWs are uniformly dispersed on FTO and that MnO_2 is deposited on the surface of the AgNWs.

Fig. 4a shows the CV curves of the AgNW network, bare MnO_2, and 3D MN/w-ANN electrodes over a potential window between 0 and 1.0 V at a scan rate of 5 mV s^{-1}. The CV curve of the pure AgNWs is almost a straight line, indicating that the contribution of pure AgNWs is insignificant.[12] The CV curve for the 3D MN/w-ANN electrode shows a much larger enclosed area than that of the bare MnO_2 electrode. Its curve exhibits obvious pseudocapacitance features with one pair of well-defined redox peaks, suggesting that the capacitance characteristics are controlled by the Faradaic redox reaction related to Mn–O/Mn–O–OH associated with Na^+ cation or OH^- anions. The specific capacitances of the 3D MN/w-ANN and the bare MnO_2 attain 551.3 F g^{-1} and 226 F g^{-1}, respectively, at a scan rate of 5 mV s^{-1}. The larger specific capacitance for the 3D MN/w-ANN electrode may be attributed to the larger surface area of the MnO_2 nanorods and the high conductivity of the AgNW network. Furthermore, the CV curves of the bare MnO_2, the MnO_2/Ag-nanowire-network without the welding treatment (MN/ANN), and the 3D MN/w-ANN electrodes were recorded at various scan rates from 5 mV s^{-1} to 100 mV s^{-1} (Fig. S4a–c, ESI†). Fig. S4d (ESI†) shows the specific capacitance of these electrodes at different scan rates. Significantly, the 3D MN/w-ANN electrode yields the highest specific capacitance. Compared with the MN/ANN electrode, it shows a good rate capability when the scan rate increases from 5 mV s^{-1} to 100 mV s^{-1}. Fig. S5 (ESI†) displays the GCD curves of the 3D MN/w-ANN electrode at currents from 0.125 mA to 1 mA. Good symmetry and fairly linear slopes are observed, indicating a superior reversible

redox reaction.[20] Lower sheet resistance and greater surface area of the MnO_2 nanomaterials and current collector materials are very important. As shown by the two black lines in Fig. 4b, the sheet resistance of the AgNW/FTO substrate decreases from 15.7 Ω sq^{-1} to 7.6 Ω sq^{-1} with increasing spin-coating time to 100, and is further decreased to 6.6 Ω sq^{-1} when the AgNW network is annealed. The red line (Fig. 4b) shows the relationship between AgNW spin-coating number and specific capacitance of the composites, which suggests that the optimum spin-coating number is ~80 times. The corresponding mass ratio between the MnO_2 and AgNW network of the sample is about 1 : 0.40 (Table S1, ESI†). Further understanding of ion diffusion in the electrode has been obtained by EIS measurement within a frequency range of 100 kHz to 0.01 Hz for the 3D MnO_2/a-AgNW and the bare MnO_2 electrodes (Fig. 4c). The 3D MnO_2/a-AgNW electrode has a much smaller charge transfer resistance than that of the bare MnO_2 electrode, which indicates that the conductivity for the 3D MnO_2/a-AgNW composite is enhanced by the AgNW network, leading to its superior capacitance behavior.

Fig. 4d shows the cycle performance of the bare MnO_2, the MN/ANN, and the 3D MN/w-ANN electrodes at 0.5 mA. From the red line, it can be seen that the specific capacitance of the bare MnO_2 electrode continuously decreases from 260.7 F g^{-1} to 130.7 F g^{-1}. However, the MnO_2 material peels off when the cycling life is only about 3600 cycles, and its specific capacitance returns to ~50%. The black line shows that after annealing the AgNW network, the specific capacitance of the 3D MN/w-ANN electrode decreases from 423.5 F g^{-1} to 370.8 F g^{-1} in the initial 400 cycles. Then, it increases up to 663.4 F g^{-1} with increasing cycle number, revealing 156.6% retention. Meanwhile, the morphology of MnO_2 gradually changes from flower-like nanorods (Fig. 3d) to lamellar wrinkles at 3000 GCD cycles (Fig. 4e), and to highly porous honeycomb-like nanoflakes when it reaches 7000 cycles (Fig. 4f). Such porous honeycomb-like nanostructures provide a much larger accessible area of Na cation. The morphology changes can be attributed to an electrochemical oxidation process during GCD cycling, leading to dissolution and redeposition of the MnO_2 electrode, which can also promote the electrolyte to diffuse into the electrode.[21–23] However, the specific capacitance of the MN/ANN electrode sharply decreases from 625 F g^{-1} to 131 F g^{-1} before the 300th cycle because of easy exfoliation of the AgNW network, revealing poor stability (blue curve in Fig. 4d). Fig. S6 (ESI†) shows photo images of the MN/ANN and the 3D MN/w-ANN electrodes after GCD testing. Compared with the 3D MN/w-ANN electrode, the MN/ANN electrode clearly peels off after the GCD cycle.

In summary, a 3D MN/w-ANN composite, with high capacitive performance and good stability, was fabricated as an electrode material of SCs. MnO_2 nanorods were grown directly on the AgNW network by an electrochemical deposition method. The AgNWs can be welded to each other at 300 °C to prevent the AgNW network from peeling off, which dramatically improves the conductivity and lifetime of the electrode. The 3D MN/w-ANN electrode also shows an ever-increasing specific capacitance from 423.5 F g^{-1} to 663.4 F g^{-1} because of gradual morphology changes from flower-like to honeycomb-like MnO_2 with increasing cycle number, revealing 156.6% retention after 7000 cycles of GCD.

This work is supported by the National Natural Science Foundation of China (No. 11404138, 51401239, 21477047), Shandong Provincial Natural Science Foundation of China (No. BS2014CL019, ZR2013BL002).

Notes and references

1 P. Simon and Y. Gogotsi, *Nat. Mater.*, 2008, **7**, 845.
2 P. Simon, Y. Gogotsi and B. Dunn, *Science*, 2014, **343**, 1210.
3 H. Xia, C. Y. Hong, X. Q. Shi, B. Li, G. L. Yuan, Q. F. Yao and J. P. Xie, *J. Mater. Chem. A*, 2015, **3**, 1216.
4 S. H. Yang, X. F. Song, P. Zhang and L. Gao, *ACS Appl. Mater. Interfaces*, 2013, **5**, 3317.
5 C. Wei, L. H. Yu, C. L. Cui, J. D. Lin, C. Wei, N. Mathews, F. W. Huo, T. Sritharan and Z. H. Xu, *Chem. Commun.*, 2014, **50**, 7885.
6 T. Zhai, S. L. Xie, M. H. Yu, P. P. Fang, C. L. Liang, X. H. Lu and Y. X. Tong, *Nano Energy*, 2014, **8**, 255.
7 H. Z. Chi, Y. W. Li, Y. X. Xin and H. Y. Qin, *Chem. Commun.*, 2014, **50**, 13349.
8 B. Zhang, W. Li, J. Sun, G. He, R. Zou, J. Hu and Z. Chen, *Mater. Lett.*, 2014, **114**, 40.
9 S. J. Zhu, J. Q. Jia, T. Wang, D. Zhao, J. Yang, F. Dong, Z. G. Shang and Y. X. Zhang, *Chem. Commun.*, 2015, **51**, 14840.
10 L. B. Ma, X. P. Shen, Z. Y. Ji, G. X. Zhu and H. Zhou, *Chem. Eng. J.*, 2014, **252**, 95.
11 J. M. Kim, H. Ju, A. I. Inamdar, Y. C. Jo, J. Han, H. S. Kim and H. Im, *Energy*, 2014, **70**, 473.
12 Z. N. Yu, C. Li, D. Abbitt and J. Thomas, *J. Mater. Chem. A*, 2014, **2**, 10923.
13 W. W. Liu, C. X. Lu, X. L. Wang, R. Y. Tay and B. K. Tay, *ACS Nano*, 2015, **9**, 1528.
14 J. Han, S. Yuan, L. N. Liu, X. F. Qiu, H. B. Gong, X. P. Yang, C. C. Li, Y. F. Hao and B. Q. Cao, *J. Mater. Chem. A*, 2015, **3**, 5375.
15 C. Julien, M. Massot, S. Rangan, M. Lemal and D. Guyomard, *J. Raman Spectrosc.*, 2002, **33**, 223.
16 D. S. Yu, K. L. Goh, Q. Zhang, L. Wei, H. Wang, W. C. Jiang and Y. Chen, *Adv. Mater.*, 2014, **26**, 6790.
17 R. Zhu, C. H. Chung, K. C. Cha, W. B. Yang, Y. B. Zheng, H. P. Zhou, T. B. Song, C. C. Chen, P. S. Weiss, G. Li and Y. Yang, *ACS Nano*, 2015, **5**, 9877.
18 G. N. Zhang, L. Zheng, M. Zhang, S. H. Guo, Z. H. Liu, Z. Yang and Z. Wang, *Energy Fuels*, 2012, **26**, 618.
19 J. Duay, S. A. Sherrill, Z. Gui, E. Gillette and S. B. Lee, *ACS Nano*, 2013, **7**, 1200.
20 P. Sun, Y. Wang, Q. Wu, S. Wang and S. M. Fang, *Mater. Lett.*, 2014, **137**, 206.
21 H. Xia, Y. S. Meng, X. Li, G. Yuan and C. Cui, *J. Mater. Chem.*, 2011, **21**, 15521.
22 H. Xia, M. O. Lai and L. Lu, *J. Power Sources*, 2011, **196**, 2398.
23 W. F. Wei, X. W. Cui, W. X. Chen and D. G. Ivey, *J. Power Sources*, 2009, **186**, 543.